Mars 1064 nm spectral radiance measurements determined from the receiver noise response of the Mars Orbiter Laser Altimeter

Xiaoli Sun, Gregory A. Neumann, James B. Abshire, and Maria T. Zuber

A technique was developed to compute the radiance of the scene viewed by the optical receiver of the Mars Orbiter Laser Altimeter. The technique used the detection threshold and the false detection rate of the receiver to provide a passive radiometry measurement of Mars at the 1064 nm wavelength over a 2 nm bandwidth and subkilometer spatial resolution in addition to the altimetry and active radiometry measurements. The passive radiometry measurement is shown to have a 2% or better precision and has been stable over several Martian years. We describe the principle of operation of the instrument and its calibration and assess its performance from sample orbital measurements. © 2006 Optical Society of America

OCIS codes: 120.0280, 120.5630, 280.3400.

1. Introduction

The Mars Orbiter Laser Altimeter[1–4] (MOLA) on board the Mars Global Surveyor (MGS) spacecraft[5,6] was designed primarily as a laser altimeter that measures range by means of the laser pulse's time of flight. MOLA measurements have produced a high-precision topographic map of Mars with approximately 670×10^6 individual laser pulse measurements over a period of more than one Mars year.[7] In addition to altimetry, the MOLA provides an active radiometry measurement of Mars at 1064 nm wavelength as a ratio of the transmitted and backscattered echo pulse energies. Furthermore, the MOLA was designed to permit simultaneous passive radiometry measurement of Mars by means of the receiver noise trigger rate and detection threshold. The MOLA laser pulse's time of flight and active radiometry measurements were described in detail in an earlier paper.[2] In this paper we describe the receiver model and analyze the performance of the passive radiometry measurements.

The MOLA passive radiometry measurement is accomplished by use of the receiver's false-alarm rate and the threshold setting to estimate the background light power onto the detector. The false-alarm rate, which is the number of threshold crossings per unit time that results from detector dark noise and background light, is registered by a noise counter. An onboard algorithm in the instrument's software dynamically adjusts the receiver's detection threshold to maintain a nearly constant false-alarm rate. The detection threshold level thereby tracks the background light and enables the receiver to operate at maximum sensitivity in altimetry measurement under a prescribed false-detection probability. The receiver's false-alarm rate and threshold level are included in the telemetry to permit a solution for the amount of background light entering the detector. The radiance of Mars under solar illumination can then be obtained given the receiver aperture, optical throughput, and spectral bandwidth. As the MGS orbits Mars, the MOLA functions as a single pixel imaging system, mapping the apparent surface brightness and seasonal variation over a 2 nm spectral bandwidth at 1064 nm wavelength and subkilometer spatial resolution.

The MOLA's passive radiometry measurements are unique in wavelength and spectral bandwidth compared with measurements by other imaging spectrometers. The bolometer of the Thermal Emission Spectrometer[8] (TES) on the MGS spacecraft covers the MOLA wavelength but with a much broader spectral bandwidth, from 0.3 to 2.7 μm. The
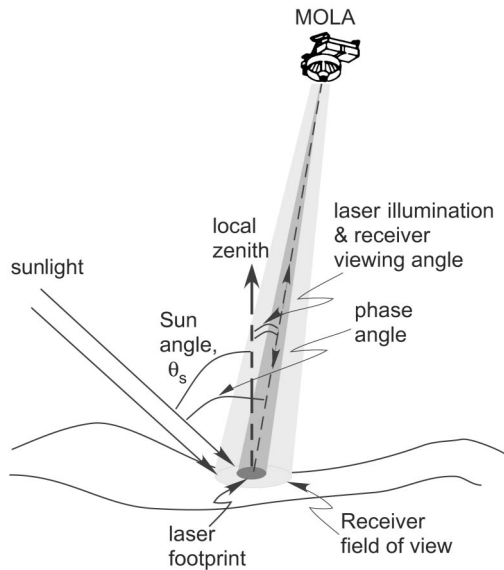
Fig. 1. MOLA measurement configuration and geometry.

Symbol	Value	Description
λ	1064 nm	Laser wavelength
A_{tel}	0.170 m^2	Receiver telescope entrance aperture area
θ_{FOV}	0.850 mrad	Receiver FOV (FWHM)
τ_{rcvr}	56.5%	Receiver optics transmission
$\Delta\lambda$	2.0 nm	Receiver optical bandwidth (FWHM)
η_d	40%	APD quantum efficiency at 1064 nm wavelength
G	120	Average APD gain
k_{eff}	0.008	APD ionization coefficient ratio
I_{ds}	15 nA	APD surface dark current
I_{db}	80 pA	APD bulk dark current
N_{amp}	(1.74 pA/Hz$^{1/2}$)^2	Preamplifier noise spectral density
R_{det}	1.26×10^8 V/W	Detector assembly responsivity
α_{thre}	1.28	Threshold scaling factor for channel 2
BW_{3dB}	5.54 MHz	Receiver noise bandwidth for Channel 2 (scaling factors and bandwidths for other channels can be found in Ref. 2)

Thermal Emission Imaging System (THEMIS) on the Mars Odyssey mission does not have a spectral band covering the 1064 nm wavelength. The spatial and temporal resolutions of MOLA radiometry measurement are also higher and may be used to produce maps of infrared brightness at higher resolution. Although the MOLA passive radiometry measurements are not calibrated in absolute terms, they are remarkably stable and repeatable, as indicated by measurements over areas where surface albedo does not change with time. These characteristics, combined with the high spatial resolution, make the observations particularly well suited for characterization of seasonal albedo changes on Mars, such as those that are due to frost deposition and sublimation and to dust movement.[9–12] In a particularly novel application, the MOLA passive radiometry data were used to track the shadow of Phobos, the innermost natural satellite of Mars, on the Martian surface to determine its orbit position and the precise time. The results were then used to refine the knowledge of Phobos's secular acceleration and accompanying gravitational tidal effects.[13]

MOLA's passive radiometry data have been collected from the beginning of the MGS mission, but the data analysis was limited to monitoring the instrument's operation and optimizing the receiver's performance during the MGS prime mapping mission. Although the MOLA performance analysis during this time revealed that the MOLA's passive radiometry measurements had scientific utility, these measurements were not a primary data product of the MGS mission because the TES on the same payload was designed primarily to map the spectral brightness of Mars. A full analysis of the MOLA passive radiometry data was carried out after the MGS prime mapping mission, which further revealed the scientific significance of the instrument and justified

its continuous use after the altimetry measurement function had ceased.

2. Mars Orbital Laser Altimeter Receiver and Solar Background Radiance

The MGS spacecraft orbits Mars in a near-polar, Sun-synchronous, nearly circular orbit at approximately 400 km mean altitude. The MOLA receiver's bore sight is fixed and normal to the spacecraft's payload deck. Figure 1 shows a simplified diagram of the MOLA measurement configuration and light paths to the receiver. The MOLA receiver parameters are summarized in Table 1. The MOLA receiver's field of view (FOV) is co-aligned with the laser beam and covers an area larger than the laser beam's footprint. The receiver telescope collects photons from the reflected laser light and sunlight scattered from the Mars surface and atmosphere within the receiver's FOV. The laser light is pulsed and is filtered out temporally. The background light is continuous and causes the detector noise to rise whenever the MGS is on the sunlit side of the planet.

Background light power P_0 incident onto the MOLA telescope can be written as

$$P_0 = I_{\text{Mars}}\Delta\lambda\eta_{\text{rcvr}}\pi\left(\frac{\theta_{\text{FOV}}}{2}\right)^2 A_{\text{tel}}, \qquad (1)$$

where I_{Mars} is the Mars radiance in watts per unit area, unit bandwidth, and unit solid angle subtended by the MOLA receiver; $\Delta\lambda$ is the receiver's optical

bandwidth; η_{rcvr} is the receiver optics transmission; θ_{FOV} is the receiver's field of view; and A_{tel} is the receiver telescope aperture area. Because the receiver parameters are known, P_0 can be calculated from the radiance of Mars and vice versa.

The average receiver false-alarm rate is a predictable function of the background light and the threshold setting over the entire dynamic range of observations. Figure 2 shows an example of how the MOLA average receiver false-alarm rate varied with the detection threshold at several background light levels. These data were obtained from a special MOLA diagnostic test on 13 September 2001, during which the threshold levels were commanded to step through a series of settings while the false-alarm rate was monitored as the MGS orbited from night into Martian daylight. The prelaunch dark-noise data are also plotted as a baseline under zero background light. These data show that the false-alarm rate can vary over several decades at a given threshold setting in response to the changing background light from Mars. Likewise, the threshold level can vary from 50 to 125 mV from nighttime to daytime.

Optical radiance measurements are usually expressed in terms of the radiance factor, or I/F, which is defined as the ratio of the measured radiance I to the radiance F of an ideal diffusive surface in vacuum with 100% reflectance under the same solar illumination. An ideal diffusive surface (Lambertian) scatters the incident light uniformly into 2π sr, and the spectral radiance at any observation angle can be written as $I_0 \cos(\theta_s)/\pi$, where I_0 is the solar irradiance ($\mathrm{W\ m^{-2}\ \mu m^{-1}}$) and θ_s is the angle between the incident sunlight and the local zenith, as indicated in Fig. 1. The radiance factor can be written as

$$I/F = \frac{\pi I_{\mathrm{Mars}}}{I_0 \cos(\theta_s)}. \qquad (2)$$

The solar irradiance is well known and has varied by only 0.5% over the past 100 years.[14] The solar irradiance at a 1064 nm wavelength is 647 mW m^{-2} nm^{-1} at 1 astronomical unit,[15] or 279 mW m^{-2} nm^{-1} at Mars's mean solar distance. As Mars orbits the Sun with eccentricity $e = 0.0934$, the solar irradiance varies by the square of the Mars solar distance, or from 82% to 122% of its mean value during a Mars year. The phase angle, the angle between the light source and the observer's line of sight, varies as the spacecraft orbits the planet and can be calculated from the spacecraft's attitude and navigation data.

The major differences between MOLA's passive and active radiometry measurements lie in the effects of atmosphere and the angles of illumination and observation. The active radiometry measures the product of the surface reflectance and the atmospheric transmission. The passive radiometry measures the same plus the atmospheric scattering of sunlight in the receiver field of view. On the one hand, the angle of illumination for the active radiometry measurement is close to zenith and is always opposite the direction of observa-
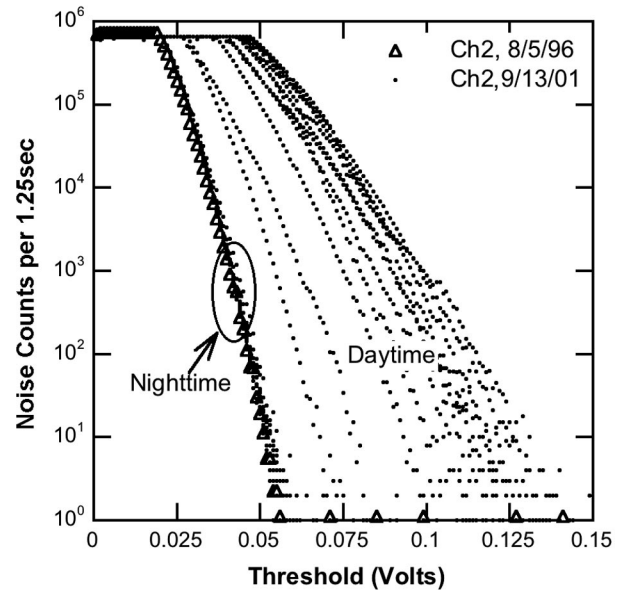
Fig. 2. MOLA channel 2 (Ch2) false-alarm rate versus threshold setting measured with the MGS in orbit around Mars on 13 September 2001. The measurements were taken as the MGS flew from the dark side of Mars to the sunlit side. The prelaunch dark-noise measurements are also plotted for comparison.

tion. In many cases, the surface may appear brighter because of the so-called opposition effect.[16] On the other hand, the angle of illumination for the passive radiometry measurement changes with the spacecraft's orbital position and local time and is rarely at opposition. These two radiometry measurements provide important data, though they are sometimes not sufficient, with which to solve for the surface reflectance and the atmospheric extinction and backscattering. They can be used with other data and physical models to improve our understanding of Mars's atmosphere and surface properties.[9]

The sampling rate of the passive radiometry measurement is determined by the integration time of the noise counters. These counters are read and reset at the end of the integration time within a 10 μs time interval. During MOLA ranging operations, the integration time was 1 s. The MOLA operated in this mode during the aerobraking and mapping mission phases spanning two Martian years.[6] Approximately five months after the MOLA achieved all the original measurement objectives and the MGS entered the extended mission, the MOLA ended the ranging operation because of failure of the clock oscillator. However, the MGS team decided to extend the MOLA operation to continue collecting passive radiometry data. The MOLA was then configured to an enhanced passive radiometry measurement mode and continues to operate to this date. In this mode the noise-counter readings are made at 8 Hz, which corresponds to an integration time of 0.125 s. The threshold levels were also lowered such that the false-alarm rate is maintained at a higher value. This improves measurement precision by reducing random counting error. Table 2

Table 2. Mars Global Surveyor Chronology and Mars Orbital Laser Altimeter Measurement Configurations

Beginning Date	MGS Phase	MOLA Measurement	Viewing Angle	Along-Track Radiometry Resolution
7 November 1996	Launch			
11 September 1997	Orbit insertion			
15 September 1997	Aerobraking	Laser ranging		
3 March 1999	Prime mapping	Laser ranging	0° (nadir)	
		Active radiometry	0° (nadir)	0.15 km diameter, 0.3 km spacing
		Passive radiometry (Same as above)	0° (nadir)	0.34 × 3 km,
31 January 2001	Extended mission			
30 June 2001		MOLA clock oscillator anomaly and investigations	18°	0.34 × 0.5 km
10 October 2001		Enhanced passive radiometry (Measurement continued to this date)		

gives a complete timeline of MGS and MOLA operations along with the radiometry measurement configurations.

The MOLA has operated nearly continuously in the enhanced passive radiometer mode since 10 October 2001. At 400 km orbital altitude the detector's FOV covers an ~340 m diameter circle on Mars's surface. At the MGS ground track speed of 3 km s^{-1}, a 0.125 s sampling interval corresponds to an along-track distance of 375 m, which gives a spatial resolution of ~0.5 km when it is convolved with the receiver's FOV. The cross-track resolution depends on the total number of tracks used in forming the image. The MGS orbital period is ~1 h and 58 min, and there are 8400 tracks over a Martian year with a track spacing of ~3 km at the equator.

3. Converting the Receiver's False-Alarm Rate and Threshold Level to Incident Optical Power

The key to passive radiometry measurement is an algorithm that converts the receiver's false-alarm rate and threshold level to the power of the background light on the detector. We developed the algorithm by improving the receiver's noise model and by calibrating it with the prelaunch and in-orbit test data.

A simplified block diagram of the MOLA receiver is shown in Fig. 3 for the instrument parameters given in Table 1. Details of MOLA laser ranging and active radiometry measurement were described previously.[1,2,7] The components that are involved with the passive radiometry measurement are a detector, a postamplifier, low-pass filters, threshold comparators, and the counters that monitor the false-alarm rates. The MOLA receiver does not directly measure the photocurrent as in a conventional radiometer. Instead, it measures the rate of the detector's noise threshold crossings, which is proportional to the integral of the probability-density function of the detection noise above the threshold.

The MOLA receiver was designed to adjust its detection threshold dynamically according to the Neymann–Pearson detection criterion,[17] in which

the detection threshold is set to a predetermined value. False alarms are caused by both the inherent detector dark noise and the quantum noise from the background light illuminating the detector. The false-alarm rate is determined by the probability-density function (PDF) of the detector noise and the detection threshold. The detector dark noise is known from preflight tests and has changed little on orbit. Therefore changes in the false-alarm rate are caused solely by the amount of background light and the detection threshold. The background light can be found uniquely from the false-alarm rate and the detection threshold level based on the receiver model and the noise distribution functions.

The average number of false alarms expected from the MOLA receiver within a counting gate interval can be written as

$$N_{\mathrm{fa}} = T_g/T_{\mathrm{fa}}, \tag{3}$$

where T_g is the gate interval and T_{fa} is the average time between adjacent false-alarm events. The average rate of false alarms, T_{fa}^{-1}, is related to the probability of a false alarm at a given time as (Ref. 17, p. 31)

$$p_{\mathrm{fa}} = \tau_W/T_{\mathrm{fa}}. \tag{4}$$

Here τ_W is the width of a noise pulse above the detection threshold and can be approximated as $\tau_W \approx 1/BW_{\mathrm{3dB}}$, where BW_{3dB} is the receiver bandwidth at the -3 dB response point ($1/\sqrt{2}$ in signal amplitude). For bandwidth-limited white noise, the occurrences of false alarms are statistically independent and the number of false alarms within a given time interval follows a Poisson distribution.

The probability of a false alarm at a fixed time can be written as

$$p_{\mathrm{fa}} = \int_{y_t}^{\infty} p(y)\mathrm{d}y, \tag{5}$$

where $p(y)$ is the PDF of the instantaneous noise.
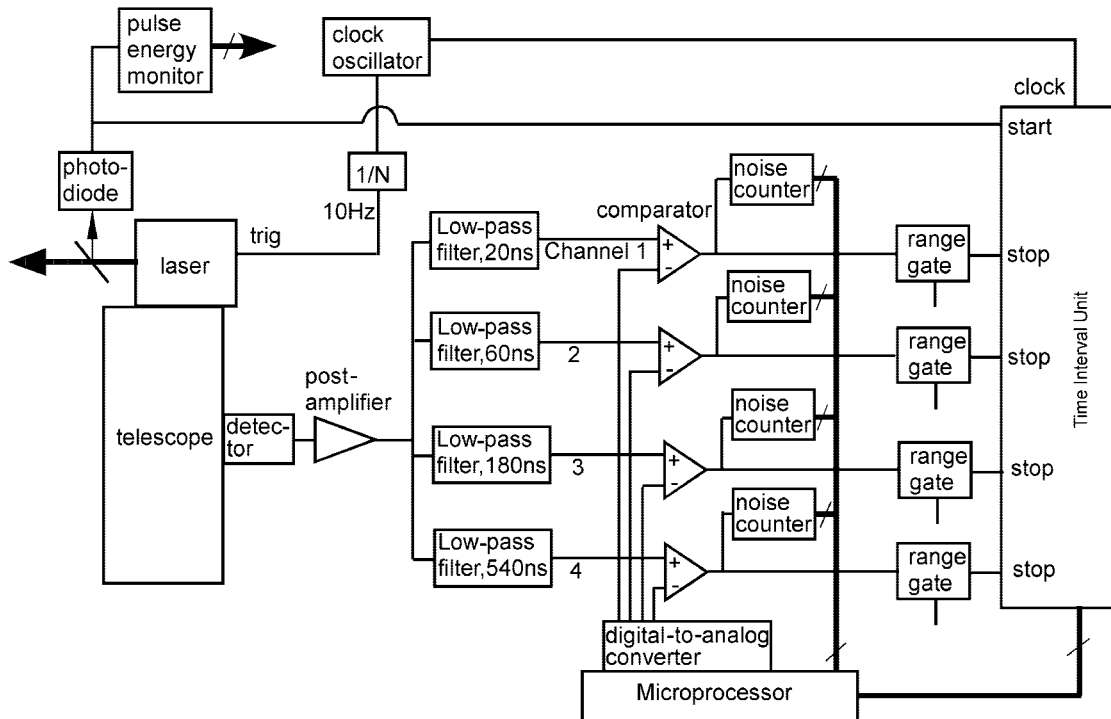
Fig. 3. Simplified MOLA block diagram.

The noise from the MOLA detector is the sum of the shot noise from the photodetector and the electrical noise of the preamplifier, which are statistically independent and have different distributions. The PDF of the total noise can be written as the convolution of the PDFs of the preamplifier circuit noise, $p_c(x)$, and that of the photodetector shot noise, $p_d(x)$, as

$$p(y) = \int_{-\infty}^{\infty} p_c(y - x)p_d(x)\mathrm{d}x. \tag{6}$$

For convenience, we define the integration variables x and y in units of the number of equivalent photoelectrons at the input to the preamplifier within the receiver integration time.

The MOLA uses a silicon avalanche photodiode (APD) as the photodetector. The PDF of the detector noise can be approximated as[18]

$$p_d(x) =$$

$$\frac{1}{(2\pi G^2 F\bar{n}_e)^{1/2}\{1 + [(x - Gn_e)(F - 1)]/GF n_e\}^{3/2}}$$
$$\times \exp\left(\frac{-(x - G\bar{n}_e)^2}{2G^2 F\bar{n}_e\{1 + [(x - Gn_e)(F - 1)]/GF n_e\}}\right),$$
$$\tag{7}$$

where G is the average APD gain; F is the excess noise factor; and $\bar{n}_e$ is the average number of the detected photons, or the primary photoelectrons, over

the integration interval. The excess noise factor can be calculated as

$$F = k_{\text{eff}}G + \left(2 - \frac{1}{G}\right)(1 - k_{\text{eff}}), \tag{8}$$

where k_{eff} is the ratio of the ionization coefficients of holes and electrons in the APD. The mean and the standard deviation, respectively, of the APD output are given by

$$\bar{x} = G\bar{n}_e, \tag{9}$$

$$\sigma_d^2 = FG^2\bar{n}_e. \tag{10}$$

The average number of primary photoelectrons is given by

$$\bar{n}_e = \left(\frac{\eta_{\text{APD}}P_0}{hc/\lambda} + \frac{I_{\text{db}}}{q}\right)\tau_n, \tag{11}$$

where n_{APD} is the APD quantum efficiency, P_0 is the received optical power, h is Planck's constant, c is the speed of light, λ is the wavelength, I_{db} is the APD bulk leakage (dark) current, q is the electron charge, and τ_n is the equivalent receiver noise integration time.

The other source of noise in the receiver is preamplifier noise, which can be modeled as a zero-mean, Gaussian random variable. The standard deviation of the preamplifier noise can be estimated more conveniently from the frequency domain by use of the spectral noise density, which can be directly measured.

The total noise variance can be obtained by integration of the noise spectrum over the noise bandwidth. For an ideal integrator, the integration time is related to the one-sided noise bandwidth, BW_n, as

$$\tau_n = \frac{1}{2BW_n}. \tag{12}$$

The electronic filters in the MOLA receiver are not ideal integrators, and their frequency responses can be approximated as five-pole Bessel low-pass filters. The noise bandwidth is related to the 3 dB bandwidth by $BW_n = 1.04 \times BW_{3dB}$, from the definition of the noise integration time in Eq. (12). The standard deviation of the integrated noise can be written as

$$\sigma_c^2 = (I_c^2 + 2qI_{ds})BW_n\left(\frac{\tau_n}{q}\right)^2 = \left(\frac{I_c^2}{2q^2} + \frac{I_{ds}}{q}\right)\tau_n, \tag{13}$$

with I_c^2 being the one-sided preamplifier input noise spectral density (A^2/Hz) and I_{ds} being the APD surface leakage current (A).

Substituting Eqs. (6), (7), (9), and (10) into Eq. (5), exchanging the order of the double integrals, and using the standard complementary error function $\mathrm{erfc}(u) = (2/\sqrt{\pi})\int_u^\infty \exp(-t^2)\mathrm{d}t$, we can rewrite Eq. (5) as

$$p_{fa} = \int_{-\infty}^{\infty} \frac{1}{2} \, \mathrm{erfc}\left(\frac{y_t - x}{\sqrt{2}\sigma_c}\right)$$
$$\times \frac{\exp\left(\frac{-(x - \bar{x})^2}{2\sigma_d^2\{1+[(x-\bar{x})(F-1)G]/\sigma_d^2\}}\right)}{(2\pi\sigma_d^2)^{1/2}\{1+[(x-\bar{x})(F-1)G]/\sigma_d^2\}^{3/2}} \, \mathrm{d}x. \tag{14}$$

The average number of false alarms in a given interval can be obtained by substitution of Eqs. (4) and (14) into Eq. (3). All the parameters in Eqs. (3)–(14) are constant, except for $\bar{x}$ and σ_d, which are functions of the received optical power defined in Eqs. (9)–(11). The threshold used in Eq. (14) can be scaled from the threshold voltages in the telemetry, v_{th}, as

$$y_{th} = \left(\tau_n \frac{\eta_d G}{hc/\lambda} \frac{a_{thre}}{R_{det}}\right)v_{th}, \tag{15}$$

where R_{det} is the detector's responsivity (V W^{-1}) and a_{thre} is the scaling factor from the detector assembly output to the comparator input of the appropriate channel. Other MOLA instrument parameters relevant for the passive radiometry measurement are given in Table 1.

The number of false alarms per unit time, the threshold level, and the received optical power are all monotonic functions of one another, and a unique solution can be found for any one of them given the
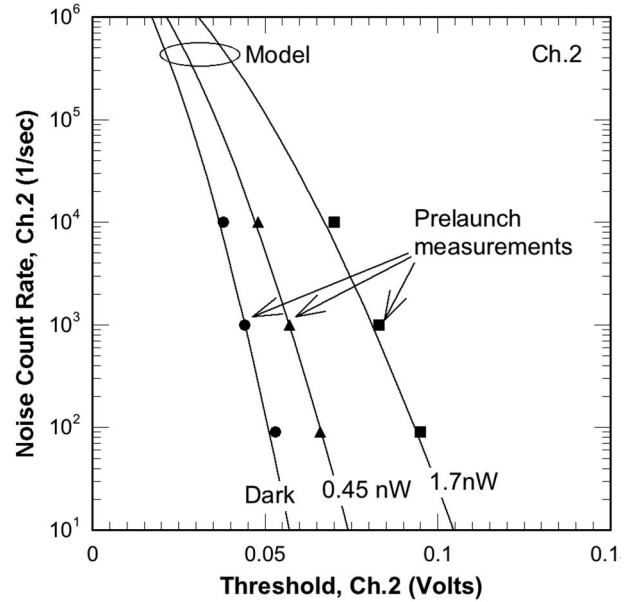
Fig. 4. Comparison of MOLA receiver model and the measured channel 2 false-alarm rate as a function of threshold levels and incident background light level.

other two. A numerical method, such as a lookup table, may be used to give the background light power as a function of the threshold level and the false-alarm rate, which we denote $f(v_{th}, N_{fa})$. Once the received optical power is found, the Mars radiance factor can be obtained from Eq. (1).

4. Calibration

The MOLA receiver was calibrated by use of data from prelaunch testing. In one of these tests, the background light levels were simulated at known levels by the MOLA ground support equipment, and the false-alarm rates were measured as a function of the threshold level.

Figure 4 shows a plot of the calculated noise-count rate versus threshold level for several values of background light. The measured data from prelaunch testing are also plotted. Three receiver parameter values were refined from those given in the earlier paper[2] to optimize the fit between theory and measurements. These parameters were the APD's quantum efficiency, from 35% to 40%; the preamplifier noise current's spectral density, from 2 to 1.74 pa/$\sqrt{\mathrm{Hz}}$; and the receiver signal's voltage gain (or threshold scaling factor), from 1.32 to 1.28. These parameter changes had little effect on MOLA altimetry performance estimates,[2] but they resulted in a significant improvement in fitting the exact shape of the noise PDFs on which the passive radiometry measurement depends. The parameter values given in Table 1 are the revised values. The original values of APD quantum efficiency and preamplifier noise density were based on the manufacturer's minimum acceptable performance specification for the batch of detectors. The revised values are closer to the typical values that we
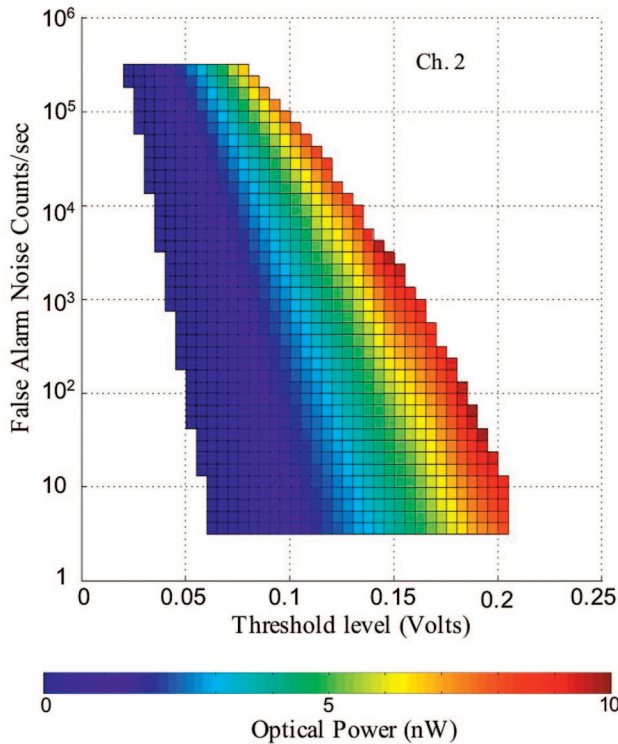
Fig. 5. MOLA channel 2 false-alarm rate versus threshold levels for background light ranging from dark to 10 nW.

found from various tests. The small adjustment in the receiver gain is well within the tolerance of the circuit components used.

Figure 5 shows a surface plot of the optical power of the background light as a function of the threshold level and the false-alarm rate. This surface plot is used as a lookup table for $f(v_{th}, N_{fa})$ in the MOLA ground data processing to yield the optical power of the background light from the observed false-alarm rate and the threshold level.

5. Measurement Precision and Accuracy

Several factors influence the precision and accuracy of the MOLA passive radiometry measurements. These include variations in the detector's responsivity owing to temperature, random fluctuations in the false-alarm rate, uncertainty in the threshold level, and the slow drift in the receiver's dark-noise level and threshold voltage.

The receiver's parameter values described in Section 4 were for room-temperature conditions. However, under different operating conditions during flight, the detector's temperature can vary from 0 °C to 40 °C. The Si APD's bias voltage is internally temperature compensated to maintain a nearly constant responsivity over this temperature range. As the temperature decreases, the APD's quantum efficiency at the 1064 nm laser wavelength decreases. The temperature compensation circuit then raises the APD's gain to keep the overall responsivity constant to within ±10%. The increase in APD gain causes the detector noise and the false-alarm rate to rise. The

temperature coefficient was determined from laboratory measurements of a similar detector assembly that contained a Si APD chip from the same batch and a bias compensation circuit identical to that in MOLA. It was found that the temperature effects on the passive radiometry measurement can be corrected by a linear function as

$$P_0 = (0.66 + 0.0097T_d)f(v_{th}, N_{fa}), \quad (16)$$

where T_d is the detector case temperature in degrees Celsius and $f(v_{th}, N_{fa})$ refers to the function of background light versus threshold and false-alarm rate at a nominal detector operating temperature (35 °C).

The detector case temperature in MOLA is not directly measured but can be inferred from the detector assembly interface plate temperatures, which are contained in the telemetry data. The detector assembly is thermally connected to the interface plate through the lens barrel. Because the Si APD's responsivity is greater at higher temperature, it was warm biased with the use of low thermal conductivity media between the detector case and the lens barrel. The power dissipation of the detector keeps the detector's temperature higher than that of the surrounding materials. The detector subsystem can be modeled as a three-node cascade thermal system. Prelaunch thermal-vacuum tests of the detector assembly showed that the APD case temperature, T_d, was 7.25 °C higher than that of the lens barrel, T_m, and 12.5 °C higher than that of the interface plate, T_i, at steady state. Neglecting radiative heat transfer, we can relate steady-state temperatures by the following equation:

$$Q = k_1(T_d - T_m) = k_2(T_m - T_i), \quad (17)$$

where Q is the heat generated by the detector module (~1.25 W) and k_1 and k_2 represent the thermal conductivities of the detector's circuit board and mounting fixture, respectively.

In flight the actual APD temperature change lags behind the changes in T_i by a significant amount owing to thermal inertia of the detector case, the lens barrel, and the interface plate. For the three-node thermal system, the instantaneous temperatures are related by a coupled pair of differential equations:

$$\dot{T}_d = \frac{Q - k_1(T_d - T_m)}{c_d}, \quad (18)$$

$$\dot{T}_m = \frac{k_1(T_d - T_m) - k_2(T_m - T_i)}{c_m}, \quad (19)$$

where $\dot{T}$ denotes the time derivative of temperature and c_d and c_m are constants. Values of k_1 and k_2 may be obtained from Eq. (17), and we obtained $c_d = 103.5$ and $c_m = 433.5$ J/°C by fitting the transient temperature data from the prelaunch tests.

The response-time delay constants for this three-node system are ~2400 and ~450 s, comparable to
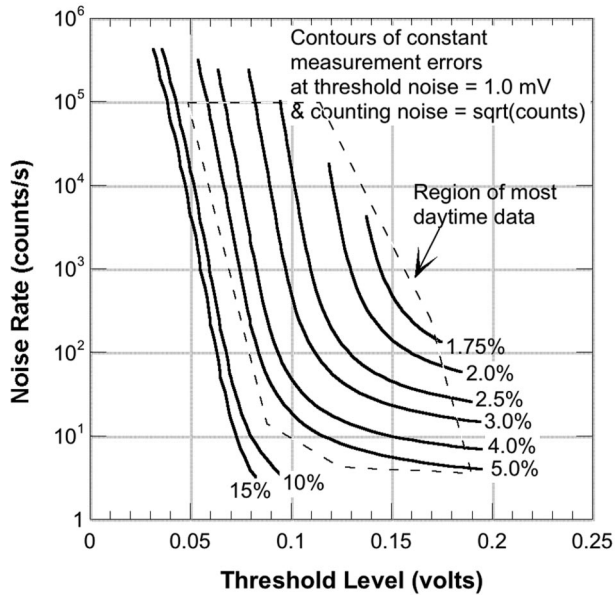
Fig. 6. Contour plot of relative error (standard deviation of the mean) in MOLA passive radiometry measurements.

the time scales of orbital changes in the thermal environment. These time constants were also consistent with our observations in flight when the MOLA experienced sudden temperature changes owing to spacecraft operation. The instantaneous detector case temperature can be obtained by numerical integration of Eq. (17) through Eq. (19).

The detector's dark noise also varies with temperature and is automatically measured when the spacecraft is over the night side of Mars. For small changes in temperature, the effect can be approximated as a small offset in the effective detection threshold given as a linear function of the detector case temperature.
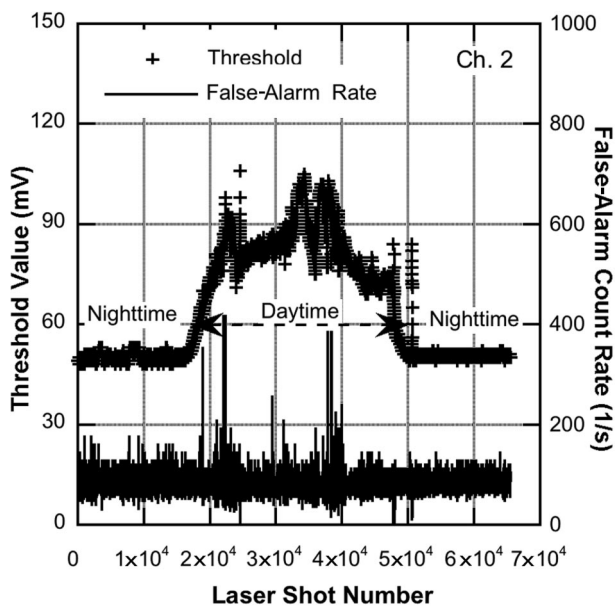
Fig. 7. Sample MOLA threshold and false-alarm count rates in normal ranging mode. Data taken on 29 June 2001 (orbit 20,316).
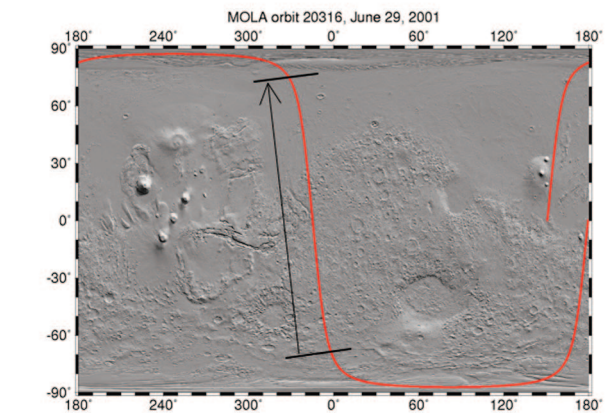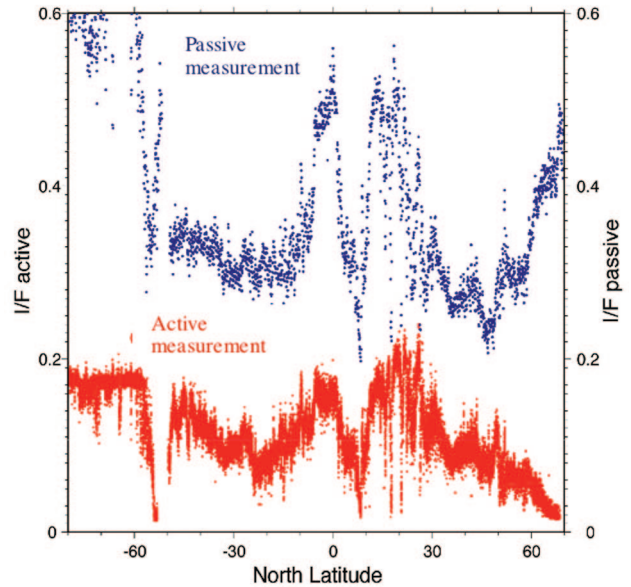
Fig. 8. Mars radiance factor from MOLA channel 2 passive radiometry measurement and active radiometry measurement for the day side of orbit 20,316 on 29 June 2001. The difference in I/F is caused by the backscattering and attenuation of dust in the atmosphere carried as part of a nascent dust storm.

The effective threshold, v_{eth}, can be written as

$$v_{eth} = v_{th} - (a_0 + a_1 T_d), \qquad (20)$$

with v_{th} given in Eq. (15). For channel 2 the offset coefficients are estimated to be $a_0 = 3.60 \times 10^{-3}$ V and $a_1 = 3.13 \times 10^{-5}$ V/°C.

The false alarms are random, relatively low rate, and uncorrelated events, which can be modeled as a Poisson random process. The variance of the number of false alarms over a given time interval can be approximated by the number of the observed false alarms. When the MOLA was in its altimetric laser ranging mode, the false-alarm rate was held at ~100/s, so the probability of a false alarm within the 20 km nominal range gate interval (133 μs) was less than 1%. The standard deviation of the measurement error in the false-alarm rate was, therefore, ~10%. During the enhanced radiometry mode operation, the thresh-

(a) HST
1042 nm

(b) MOLA
1064 nm
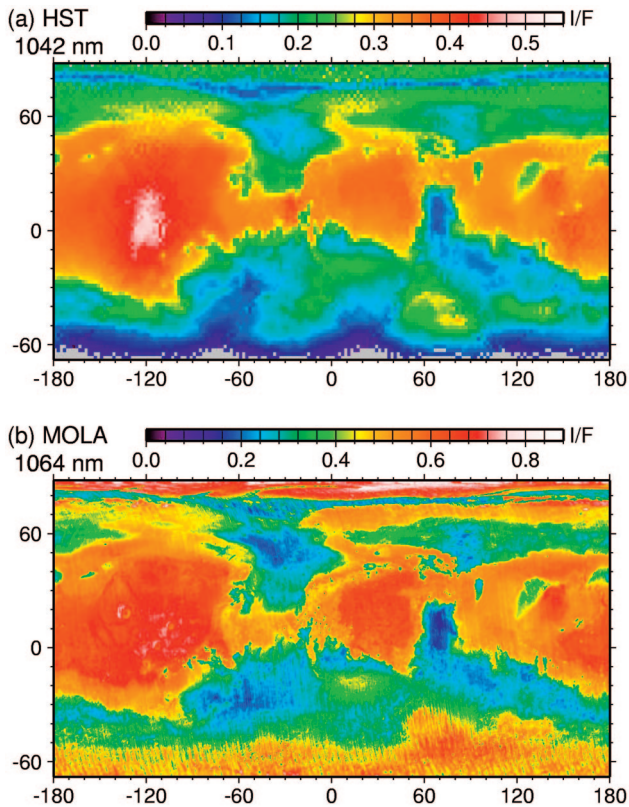
Fig. 9. Images of Mars from the HST and by MOLA passive radiometry measurement. The HST image was taken by the Wide Field Planetary Camera 2 (WFPC2) at 1044 ± 31 nm wavelength at a resolution of 20–30 km per pixel and a solar illumination angle of ~3°. The MOLA measurement had an along-track spatial resolution of 3 km and orbit spacing of 3 km at the equator.

Fig. 10. Average radiance factors of two 2.5° × 5° regions shown in Fig. 11 versus the seasonal longitude of the Sun (L_s, angular position of the planet in its orbit around the Sun with 0° chosen to be the northern vernal equinox). The data were collected from the commencement of the mapping phase, March 1999–December 2004.

old level was lowered to give ~10,000/s false alarms, so the random counting error was reduced to ~1%.

The uncertainty in the threshold level comes mainly from the inherent circuit noise at the comparator inputs and from the quantization error in digital-to-analog converter (DAC) output. The standard deviation of the inherent circuit noise was assumed to be 1 mV, which was typical for this type of circuit. The quantization error of the DAC may be modeled as a uniformly distributed random variable over the DAC step size. The DAC step size for MOLA threshold voltage generation is 1 mV. The standard deviation is $1/\sqrt{12}$ mV. The circuit noise and the quantization noise are independent of each other, and the standard deviation of the combined circuit noise is $[1^2 + (1/\sqrt{12})^2]^{1/2} = 1.04$ mV.

The standard deviation of the error in the background light measurement that is due to fluctuations in the false-alarm count and to circuit noise can be approximated as

$$\sigma_P = \left[\left(\frac{\partial P_0}{\partial y_{th}} \sigma_{y_{th}} \right)^2 + \left(\frac{\partial P_0}{\partial N_{fa}} \sigma_{N_{fa}} \right)^2 \right]^{1/2}, \quad (21)$$

where σ_{th} is the standard deviation of the threshold (circuit) noise and $\sigma_{N_{fa}}$ is the standard deviation of the

number of false alarms, equal to the square root of the observed number of false alarms within the integration time. Partial derivatives $\partial P_0/\partial y_{th}$ and $\partial P_0/\partial N_{fa}$ can be determined from the slope of the surface plot shown in Fig. 5 along the horizontal and vertical axes, respectively. Figure 6 shows the resultant normalized radiometry measurement error, defined as the ratio of the standard deviation to the mean. It shows that the majority of the measurement data have relative errors of <5%. Measurements over low- to mid-latitude regions with higher than 1 nW background light onto the detector have a relative error of <2%.

During flight, the measured optical power of the background light onto the detector ranges from 0 to approximately 10 nW. In darkness, the effective noise of the measurement has an ~10 pW standard deviation per 0.125 s interval, measured over a 100 s baseline. At a typical daytime background light level, the noise level may be estimated from observations over relatively featureless terrain and is approximately 25 pW at an average incident power of ~5 nW, or 0.5%, per 0.125 s. The noise is dominated by the counting statistics, and the error may be reduced by averaging of several successive measurements at the cost of coarser spatial resolution.

One may further reduce the errors in the radiometry measurement by averaging the results from some or all four of the receiver channels. Although all the channels share the same detector as the signal source, the false-alarm rates are obtained over different electrical bandwidths and at different effective threshold levels. This means that the threshold cross-
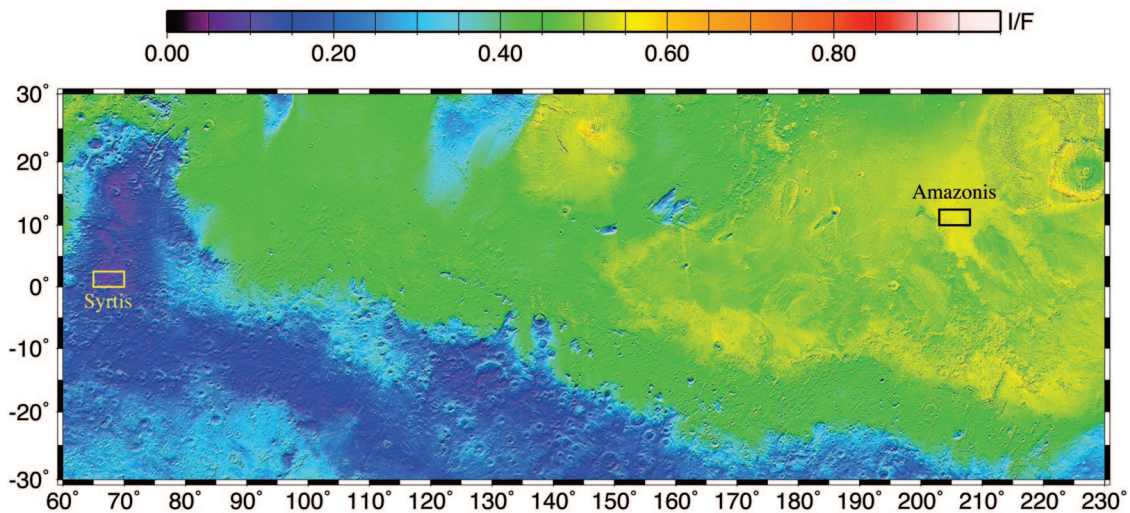
Fig. 11.   Image of Mars made solely from the MOLA passive radiometry measurements over the same period as for Fig. 10.

ings for different channels are not entirely correlated; thus, in principle, one may improve the uncertainties in the radiometry measurement by averaging them. However, low-frequency noises, such as $1/f$ noise and spacecraft power supply noise, are common to all the channels and cannot be reduced by averaging. The overall passive radiometry measurements from the MOLA were found to improve (i.e, there was less fluctuation in the along-track measurement) when the results from channels 1 and 2 but not channels 3 and 4 were averaged. Futhermore, the threshold for channel 1 was fixed near its maximum value during most of the laser ranging phase of the MOLA operation to reduce ranging error as well as receiver saturation. Therefore, only channel 2 passive radiometry measurements were available, and no averaging could be performed during that time.

We also considered the effect of space radiation on receiver performance. The MGS radiation environment was estimated to be ~7 krad(Si) total dose per Earth year during cruise and ~6 krad(Si) per Martian year with a 2.54 mm (100 mil) thick aluminum shielding. The total dose at the detector, which is the component most sensitive to radiation damage, was much lower, a few krad(Si) or less, because of the shielding provided by the materials surrounding the detector. The total doses for the sensitive electronics components should be similar or a few times higher, depending on their position. In such a moderate radiation environment, the major effects to be considered are the increase in the detector's dark current,[19] the degradation of electrical circuits, and the darkening of the optics.

The Si APD's dark noise increase owing to space radiation is estimated to be 30 pa/krad(Si),[19] which is comparable to the prelaunch APD dark current. As mentioned above, the total detector dark noise is monitored every orbit when MGS is on the dark side of Mars. We can compensate for any slow increase in dark current that is due to radiation damage by ad-

justing the threshold bias based on Eq. (20). The effects of space radiation on the electrical circuits and optics are believed to be negligible based on instrument design, parts selection, and preflight test data. The flight data shown in Fig. 2 also confirmed that there was little degradation in the MOLA detector dark noise after five years in space.

6.   Radiometry Measurements from Orbit

Examples of the MOLA threshold levels and the false-alarm count rates for channel 2 are plotted in Fig. 7 as a function of the laser shot number for an orbit around Mars on 29 June 2001 (orbit 20,316). For this orbit the MOLA was in its normal laser ranging mode and Mars was near its northern autumnal equinox. Figure 8 shows the resultant Mars radiance factor based on both passive and active radiometry measurements. The atmosphere was dusty during this time from a nascent global dust storm, which caused the radiance factor from the active radiometry to be substantially attenuated. The sunlight backscattered from the dust, however, caused the scene to be brighter in the passive radiometry measurement.

Figure 9 shows a Mars image constructed from the MOLA passive radiometry measurements over a period from March to June 1999. An image taken by the Hubble Space Telescope (HST) within the same period over a 61.1 nm optical bandwidth centered at 1042 nm (Ref. 20) is also shown for comparison. The MOLA measurements show features similar to those seen by the HST. It also reveals more features of the Mars surface, particularly near the polar regions where the lighting and the observation angles for the HST are poor. The HST measurements were taken at a Sun angle of 2.7° to 10°, whereas the MOLA measurements were taken at greater than 23° owing to the local time (2 PM) of the MGS orbit. The HST image was a snapshot over a relatively short exposure time, whereas the MOLA images were taken by scanning the planet over a 120 day period. The overall differ-

ence between the absolute values of the two was ~60%, and the exact causes of this difference are not understood. Although the MOLA passive radiometry measurements were not calibrated in an absolute sense, the instrument's precision and stability are sufficient for studying spatial and seasonal changes in Martian surface albedo.

Figure 10 plots the average radiance factors of two $2.5° \times 5°$ regions, one at Syrtis Major and the other at Amazonis Planitia, as shown in Fig. 11, as a function of the seasonal longitude of the Sun (L_s, the angular position of the planet in its orbit around the Sun, with 0° chosen to be the northern vernal equinox). The data were collected at a nadir viewing angle from the commencement of the mapping phase in March 1999 to the end of altimetric operation in June 2001, followed by operation from October 2001 to the present at an 18° forward pitch angle that we use to conserve spacecraft fuel. The sudden shift in the radiance factor in the Amazonis region midway in the plot coincided with a change in the MGS viewing angle. There is no apparent long-term downward trend besides a seasonal variation, indicating that the receiver's responsivity is stable over several Martian years.

Finally, a composite image of the Mars mid-latitude regions, including the two regions referred to in Fig. 10, is shown in Fig. 11. The image is made solely from three Martian years of MOLA passive radiometry observations, from the commencement of the MGS mapping phase to December 2004. Seasonal variations in albedo, such as those caused by annual dust storms, have been removed from individual orbital tracks. The image has been sharpened by means of along-track gradient shading (high-pass filtering). The image quality of the map from the MOLA radiometry measurements is comparable to those from medium-resolution cameras. The geolocation of each pixel is the same as that of the laser altimetry, which is much more accurate than that of an imaging system.

7. Summary

We have developed a technique for a passive radiometry measurement from the detector noise density of the MOLA receiver. The receiver's performance was stable, and the radiance measurements were repeatable over several Martian years. Over time, the MOLA passive radiometric measurement has provided a high-precision, near-infrared map of Mars over the 1064 ± 1 nm spectral range. Monitoring of the temporal variations has the potential to permit seasonal changes in the atmosphere and the cryosphere of Mars to be studied.[10–12]

References

1. M. T. Zuber, D. E. Smith, S. C. Solomon, D. O. Muhleman, J. W. Head, J. B. Garvin, J. B. Abshire, and J. L. Bufton, "The Mars Orbiter Laser Altimeter investigation," J. Geophys. Res. **97,** 7781–7797 (1992).

2. J. B. Abshire, X. Sun, and R. S. Afzal, "Mars Orbiter Laser Altimeter: receiver model and performance analysis," Appl. Opt. **39,** 2449–2460 (2000).

3. R. S. Afzal, "Mars Observer Laser Altimeter: laser transmitter," Appl. Opt. **33,** 3184–3188 (1994).

4. L. Ramos-Izquierdo, J. L. Bufton, and P. Hayes, "Optical system design and integration of the Mars Orbiter Laser Altimeter," Appl. Opt. **33,** 307–322 (1994).

5. A. A. Albee, F. D. Palluconi, and R. E. Arvidson, "Mars Global Surveyor mission: overview and status," Science **279,** 1671–1672 (1998).

6. A. L. Albee, R. E. Arvidson, and F. D. Palluconi, "Overview of the Mars Global Surveyor mission," J. Geophys. Res. **106,** 23,291–23,316 (2001).

7. D. E. Smith, M. T. Zuber, H. V. Frey, J. B. Garvin, J. W. Head, D. O. Muhleman, G. H. Pettengill, R. J. Phillips, S. C. Solomon, H. J. Zwally, W. B. Banerdt, T. C. Duxbury, M. P. Golombek, F. G. Lemoine, G. A. Neumann, D. D. Rowlands, O. Aharonson, P. G. Ford, A. B. Ivanov, P. J. McGovern, J. B. Abshire, R. S. Afzal, and X. Sun, "Mars Orbiter Laser Altimeter (MOLA): experiment summary after the first year of global mapping of Mars," J. Geophys. Res. **106,** 23,689–23,722 (2001).

8. P. R. Christensen, J. L. Bandfield, V. E. Hamilton, S. W. Ruff, H. H. Kieffer, T. N. Titus, M. C. Malin, R. V. Morris, M. D. Lane, R. L. Clark, B. M. Jakosky, M. T. Mellon, J. C. Pearl, B. J. Conrath, M. D. Smith, R. T. Clancy, R. O. Kuzmin, T. Roush, G. L. Mehall, N. Gorelick, K. Bender, K. Murray, S. Dason, E. Greene, S. Silverman, and M. Greenfield, "Mars Global Surveyor Thermal Emission Spectrometer experiment: investigation description and surface science results," J. Geophys. Res. **106**(E10), 23,823–23,871 (2001).

9. A. B. Ivanov and D. O. Muhleman, "Opacity of the Martian atmosphere from Mars Orbiter Laser Altimeter (MOLA) observations," Geophys. Res. Lett. **25,** 4417–4420 (1998).

10. M. T. Zuber and D. E. Smith, "Observations of the seasonal polar icecaps of Mars at 1064 nm," presented at the Third Mars Polar Science Conference, Alberta, Canada, 13–17 October 2003.

11. S. Byrne, M. T. Zuber, and G. A. Neumann, "Interannual and seasonal behavior of Martian residual ice-cap albedo," Planet. Space Sci. (to be published).

12. R.-R. Lu, S. Byrne, and M. T. Zuber, "Seasonal albedo changes on Mars from MOLA radiometry and TES: seeking an explanation for apparent summer snow," submitted to J. Geophys. Res.

13. B. G. Bills, G. A. Neumann, D. E. Smith, and M. T. Zuber, "Improved estimate of tidal dissipation within Mars from MOLA observation of the shadow of Phobos," J. Geophys. Res. **110**(E7), E07004 (2005).

14. C. Fröhlich and J. Lean, "Total solar irradiance variations: the construction of a composite and its comparison with models," in *New Eyes to See Inside the Sun and Stars,* F. L. Deubner, ed., International Astronomical Union Symposium 185 (Kluwer Academic, 1998), pp. 89–102.

15. J. S. Accetta and D. L. Shumaker, *The Infrared and Electro-*

Optical Systems Handbook (Environmental Research Institute of Michigan, 1993).

16. B. Hapke, *Theory of Reflectance and Emittance Spectroscopy* (Cambridge U. Press, 1993), Chap. 8.
17. M. I. Skolnik, *Introduction to Radar Systems* (McGraw-Hill, 1962).
18. P. P. Webb, R. J. McIntyre, and J. Conradi, "Properties of avalanche photodiodes," RCA Rev. **35,** 234–278 (1974).
19. X. Sun, D. Reusser, H. Dautet, and J. B. Abshire, "Measurement of proton radiation damage of Si avalanche photodiodes," IEEE Trans. Electron. Devices **44,** 2160–2166 (1997).
20. J. F. Bell III, "HST studies of Mars," in *A Decade of Hubble Space Telescope Science,* M. Livio, K. Noll, and M. Stiavelli, eds. (Cambridge U. Press, 2003), pp. 1–24.